Iranian Journal of Materials Science and Engineering, Vol. 22, Number 2, June 2025
RESEARCH PAPER

Development of Branched ZnO Microrods: A Comprehensive Structural and Optical Characterization

Ines Dhifallah*, F.I.H. Rhouma, Imen Saafi, Jamila Ben Naceur, Wafa Selmi, Wissem Dimassi, Radhouane Chtourou

* *ines.dhifallah@crten.rnrt.tn*

Laboratory of Nanomaterials and Renewable Energy Systems LaNSER, Research and Technology Center of Energy, Borj-Cedria Science and Technology Park, BP 95, 2050 Hammam-Lif, Tunisia

Received: January 2025 **Revised: May 2025** **Accepted: June 2025**
DOI: 10.22068/ijmse.3884

Abstract: *In this study, a novel three-step method for the synthesis of ZnO and branched ZnO microrods was developed. Numerous techniques were used to analyze the obtained samples: photoluminescence (PL) spectroscopy, Raman spectroscopy, Fourier transform infrared spectroscopy (FTIR), scanning electron microscopy (SEM), energy dispersive X-rays (EDX), ultraviolet-visible spectroscopy (UV-visible) and X-ray diffraction (XRD). The XRD study and Rietveld refinement confirmed that the synthesized samples have the hexagonal wurtzite structure of ZnO without any impurity, with the $P6_3mc$ space group. To further verify our experimental results, structural parameters were calculated using First Principles Density Functional Theory (DFT) calculations and compared with experimental ones. The DFT calculations and Rietveld refinement results observed a slight decrease in the unit cell volume following the branching process. Raman spectra showed peaks corresponding to the phonon modes of hexagonal wurtzite ZnO, consistent with XRD and Rietveld refinement results. SEM confirmed that ZnO and BZnO samples have hexagonal rod and branched rod shapes. BZnO showed stronger green PL emission but lower overall PL intensity than ZnO. The reduced photoluminescence (PL) intensity across all frequencies indicates enhanced separation of the photogenerated electron-hole pairs in branched ZnO (BZnO) due to decreased recombination.*

Keywords: *Branched ZnO microrods, Rietveld refinement, Structural properties, Photoluminescence.*

1. INTRODUCTION

Zinc oxide (ZnO) is a versatile semiconductor material valued for its unique properties, including a wide bandgap, high transparency, and excellent photocatalytic activity. These properties make ZnO a leader in research areas such as opto-electronics, photocatalysis and gas detection [1-4]. Among the various ZnO structures, microrods are characterized by their unique one-dimensional elongated shape [1]. This property leads to a high aspect ratio, significantly increasing their surface area. This increased surface area is critical for superior performance in applications such as gas sensing (increased sensitivity through more interaction sites for target molecules), photocatalysis (improved light absorption and reaction rates), and solar cells (improved light harvesting and charge generation) [2]. Compared to bulk ZnO, microrods provide a more efficient platform for these functionalities due to their superior light-matter interaction and larger surface area for crucial reactions [3, 4].

Ahmed et al. [5] reported the successful synthesis of high-quality zinc oxide (ZnO) microrods using a laser-assisted chemical bath deposition (LACBD) method. They investigated the potential of these ZnO microrods for detecting ultraviolet (UV) light. Encouragingly, all samples responded positively to UV light, indicating their suitability for ultraviolet (UV) light detection applications. These results opened new avenues for research on optimizing LACBD techniques to tailor ZnO microrods for improved UV detection performance. Benu et al. [6] found that the synthesis of uniform fibrous ZnO microrods was achieved using a macroemulsion-mediated solvothermal method and exhibited high photocatalytic efficiency, high photocatalytic degradation rate and high stability, which is attributed to their larger surface area, smaller band gap energy and overall defect density.

The synthesis of ZnO microrods has been extensively researched, with hydrothermal synthesis emerging as the leading method. This versatile and scalable technique enables the growth of high-quality microrods under high-pressure and high-temperature conditions. In particular, hydro-thermal synthesis offers precise control over size, shape and morphology, enabling the production of microrods with tailored properties. This control is crucial for further customization through post-

[DOI: 10.22068/ijmse.3884]

synthesis modifications such as doping [4, 7, 8], heterostructure formation [9, 10], and surface treatment [11].

In addition to the well-known advantage of a high aspect ratio for microrods, the specific morphology also has a significant influence on the functionalities [12]. For example, branched ZnO nanorod photoanodes for dye-sensitized solar cells (DSSCs) showed a remarkable five-fold increase in efficiency (2.63%) compared to traditional vertical ZnO nanorods (0.53%) [13]. Siriphongsapak et al. [14] used a hydrothermal method to grow the branched ZnO nanorods on the surface of the rod template to produce the hierarchical ZnO nanostructure. Many research groups also reported that the structural and morphological properties, including size, shape, porosity and types of defects, play a crucial role in the functional properties of ZnO [15]. Research has shown that branched ZnO microrods exhibit superior photoelectrochemical (PEC) water splitting performance compared to their one-dimensional counterparts due to their enhanced charge transport, light absorption, and improved surface area [16]. This highlights the importance of morphology control in optimizing ZnO microrods for specific applications. Developing ZnO microrods with precisely controlled morphologies is crucial for optimizing their performance in various scientific and technological applications. Complicated branched morphologies have attracted great research interest due to their potential to influence material properties in desired ways.

The present work presents a three-step synthesis method for the synthesis of branched ZnO microrods (BZnO) structures. Our aim was to investigate how branching affects the structural and optical properties of ZnO microrods. The synthesis was initiated by depositing ZnO seed layers on the fluorine-doped tin oxide (FTO) substrates. This was followed by hydrothermal growth of primary ZnO microrods, and finally, we used chemical bath deposition to create branched structures on these initial ZnO microrods.

We expect that the branching process will significantly influence the properties of the resulting ZnO microrods. In our study, we used various characterization techniques to understand the relationship between branching and material properties in ZnO microrods. X-ray diffraction revealed the crystal structure, while scanning electron microscopy and energy-dispersive X-ray spectroscopy provided insights into the morphology and elemental composition. Raman and Fourier transform infrared spectroscopy were used to assess the vibrational properties. Finally, ultraviolet-visible spectroscopy and photoluminescence spectroscopy were used to evaluate optical properties. Notably, this study goes beyond traditional techniques by incorporating Rietveld refinement and density functional theory calculations to provide a deeper understanding of the BZnO microrods structure. This comprehensive approach not only reveals the fundamental connection between branching and material properties but also lays the foundation for future adaptation of BZnO microrods for specific applications, including photocatalysis.

2. EXPERIMENTALS PROCEDURE

2.1. Preparation of ZnO Microrods

Fluorine-doped tin oxide (FTO)-coated glasses (1.0 cm × 2.0 cm) were sequentially cleaned in an ultrasonic bath with acetone, isopropyl alcohol, and deionized water for 15 min and then dried at room temperature.

The cleaned substrates were used to prepare the ZnO seed layer. First, the conductive side of the FTO substrate was coated with 10 µL of the zinc acetate-ethanol solution (0.01 M) at 2500 rpm with a spin coater for 30 s and then dried at 80°C for 10 min. The above step was repeated five times. The obtained substrates were annealed in an oven with an air atmosphere at 300°C for one hour. The prepared substrates were placed face-down (conductive side) into Teflon-lined stainless steel autoclaves filled with an aqueous solution of zinc nitrate hexahydrate $Zn(NO_3)_2 \cdot 6H_2O$ (0.2 M) and hexamethylene tetramine (HMTA) $C_6H_{12}N_4$ (0.1 M), and then heated. It was heated at 95°C for 8 hours. Once the autoclave had cooled, the ZnO microrods were thoroughly rinsed with deionized water to remove any impurities and then dried at 70°C to ensure optimal cleanliness of the samples.

2.2. Preparation of Branched ZnO Microrods

The BZnO microrods were prepared by the chemical bath deposition (CBD) method. The prepared ZnO microrods were vertically immersed in the solution of zinc acetate dihydrate $Zn(CH_3COO)_2(H_2O)_2$ (0.6 M) and potassium hydroxide KOH (4 M). During deposition, the

[DOI: 10.22068/ijmse.3884]

solution was heated to 30°C using a water bath with constant stirring for 5 hours. The film was removed from the bath and washed with deionized water to remove excess ZnO particles. While the three-step synthesis method in this study allows for effective control over morphology and enables the formation of well-defined branched ZnO microrods, it also poses certain challenges. These include a relatively long processing duration and the requirement for multiple synthesis steps, factors that may increase the overall complexity of the process. Furthermore, achieving consistently reproducible branching necessitates precise regulation of experimental parameters such as temperature and precursor concentrations.

2.3. Characterizations

For structural analysis, room temperature X-ray diffraction was performed using a Bruker D8 Advance X-ray diffractometer equipped with monochromatized Cu Kα radiation (λ= 1.541 Å). XRD patterns were collected with a step size of 0.02° within the 2θ angle range of 10–90°. The collected data was then refined using the FULLPROF software for further analysis. Scanning electron microscopy (Thermo Scientific Quanta 250) at 25 kV accelerating voltage was used to analyze the morphology of the samples. The elemental composition was determined using an energy-dispersive X-ray spectrometer. RAMAN spectra were registered with a Jobin Yvon HR LabRAM, registered in the spectral range 90 - 800 cm^{-1} at room temperature under a 488 nm Ar^{+} laser source. Fourier-transform infrared spectroscopy was performed on a Bruker Vertex 80/80v spectrometer (Bruker Optics Inc.) with KBr pellets in transmission mode within the range of 400–4000 cm^{-1}. Optical measurements were derived at room temperature from absorption spectra recorded with a Perkin-Elmer Lambda 950 ultraviolet-visible near-infrared spectrophotometer in the wavelength range of 325–800 nm and from photoluminescence spectra recorded with a Perkin-Elmer LS55 spectrometer at an excitation wavelength of 325 nm.

3. RESULTS AND DISCUSSION

3.1. X-ray Diffraction (XRD) Analysis

Fig. 1 shows the XRD patterns of the ZnO microrods deposited on a fluorine-doped tin oxide (FTO) conductive glass substrate before and after branching. The Branched (BZnO) and ZnO microrods were analyzed using an X-ray diffractometer with a scan rate of 2°/min in the 10–90°.

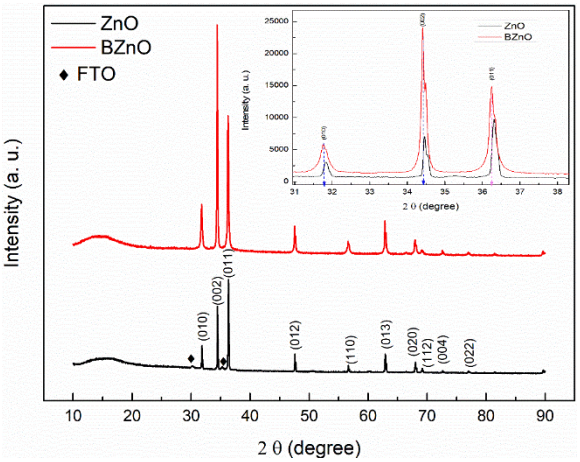

Fig. 1. X-ray diffraction patterns of ZnO and BZnO microrods

All diffraction peaks were consistent with the reference pattern for hexagonal wurtzite ZnO (JCPDS 36-1451) and did not indicate any significant impurities, except for two weak reflections corresponding to tin oxide (SnO_2) from the fluorine-doped tin oxide (FTO) substrate (JCPDS card no. 98-015-7451) [2]. The sharp and narrow diffraction peaks of the samples show that the material has good crystallization. The BZnO sample has a preferred orientation along the (002) plane along the c-axis perpendicular to the substrate direction. This indicates that the branching of the ZnO microrods improves the vertical orientation of most ZnO microrods on the substrate, so that they grow with a uniform orientation toward the (002) plane. For ZnO, the (011) diffraction peak was more intense than that of the (002) plane but of similar intensity. This proves that ZnO microrods do not grow in a uniform orientation but rather grow toward the (002) and (011) planes rather than the (010) plane. From Fig. 1, we can see the broadening, intensification, and slight shift of the peaks after branching to smaller angles, which can be clearly seen by overlaying the XRD diffractograms of the samples. This variation in the positions, intensities and widths of the peaks and orientation growth suggests a change in the crystal structure of ZnO after branching.

To gain a deeper understanding, the XRD data

[DOI: 10.22068/ijmse.3884]

was analyzed by refining the Rietveld code implemented in the FULLPROF suite [17]. Fig. 2 shows the Rietveld refinement for the ZnO and BZnO samples. The horizontal lower curve displayed at the bottom of each Rietveld profile represents the difference between the observed (Yobs) and calculated (Ycalc) diffraction peak profiles.

The good agreement between experimental and fitting diffraction lines ensures the hexagonal structure of ZnO and BZnO samples with a Space group $P6_3mc$, and there are no signs of a crystalline secondary phase that could be detected within the limits of the X-ray diffractometer. This result is consistent with the literature for the undoped sample prepared by Rhouma et al. [18], where the Zn atoms located at 2a (1/3, 2/3, 0) position and oxygen vacancy is at 2b (1/3, 2/3, z) position. By adding more ZnO during the branching process, the small peaks of the FTO substrate (see Fig. 1) disappear. Through the rietveld analysis, the determined unit cell parameters (a, b and c), the unit cell volume V, the average bond length d_{Zn-O}, the average bond angle $\theta_{Zn-O-Zn}$ and the discrepancy factors were determined and regrouped in Table 1.

The obtained values match those reported in the ref [19, 20]. Table 1 shows that the branched BZnO sample exhibits lattice compression compared to unbranched ZnO, despite the peak shift towards lower side (see Fig. 1). The volume decrease and the shift toward small angles in the XRD may likely be related to certain types of defects like zinc interstitial Zn_i and oxygen vacancies V_O induced by branching process.

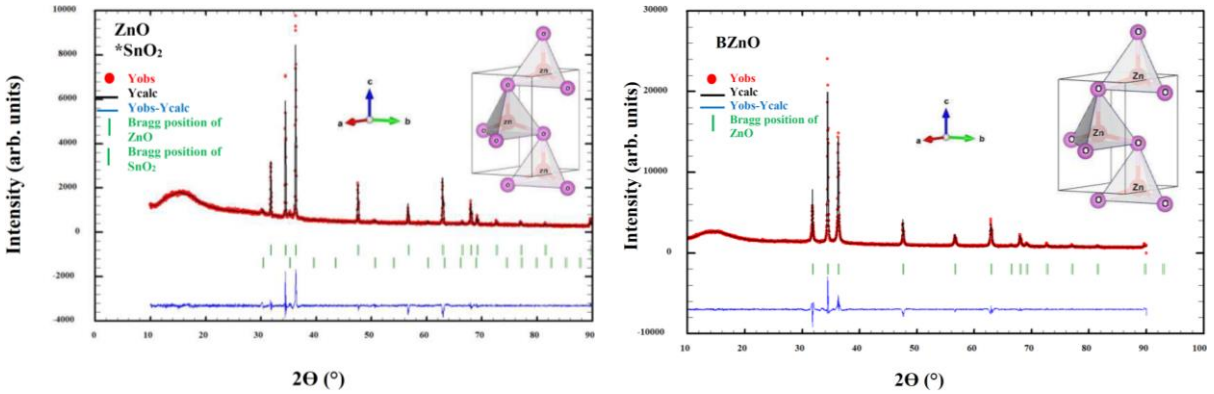

Fig. 2. Rietveld refined X-ray diffraction patterns for ZnO and BZnO microrod samples. Observed (calculated) profiles are shown by dotted (solid lines). The short vertical marks represent Bragg reflection. The lower curve is the difference plot. The inset presents the hexagonal structure of ZnO and BZnO microrods

Table 1. Refined structural and discrepancy factors parameters for ZnO and BZnO obtained following the structural refinement by the Rietveld method. a, b and c: cell parameters; V: unit cell volume; z: Oxygen position; d_{Zn-O}: distance; $\theta_{Zn-O-Zn}$: angle. Agreement factors of profile R_p, weighted profile R_{wp} and structure R_F. x^2: the goodness of fit

Parameters	ZnO	BZnO
Refined structural parameters		
$a(Å) = b(Å)$	3.24871	3.24853
$c(Å)$	5.20592	5.20424
$V(Å^3)$	47.583	47.562
$z_{Oxygen\ position}$	0.37145	0.39795
$d_{Zn-O}(Å)$	1.992	1.949
$\theta_{Zn-O-Zn}(°)$	109.6	105.8
Rietveld discrepancy factors		
$R_{wp}(\%)$	6.73	6.49
$R_{exp}(\%)$	3.77	2.74
$R_p(\%)$	4.48	4.31
$R_F(\%)$	4.42	3.12
$\chi^2(\%)$	3.19	5.61

[DOI: 10.22068/ijmse.3884]

These defects disrupt the atomic arrangement, alter lattice parameters, deform the structure, and induce lattice contraction, resulting in a shift of the XRD peaks toward smaller angles and a reduction in the unit cell volume [21].

It can be seen that the fit quality (x^2) has small residual values, confirming the good agreement between the observed and calculated XRD data, with a lower background noise (blue line) as shown in Fig. 2. Based on the parameters obtained from the Rietveld refinement of such samples, the hexagonal structure of ZnO and BZnO were determined using the program "Vesta", as shown in the inset of Fig. 2. There was significant variation in the lattice constants and volume of the hexagonal unit cell of zinc oxide between BZnO and ZnO.

The average particle size in the prepared samples is given by the Debye-Scherrer equation [22]:

$$D = \frac{k\lambda}{\beta\cos\theta} \quad (1)$$

Where D is the average crystallite size, θ represents the Bragg's angle, λ represents the wavelength of X-ray, β represents the XRD peak width at FWHM (full width half maximum) and k is known as the Scherrer constant (k= 0.94).

The obtained value of average crystallite size was 56.58 and 50.04 nm for ZnO and BZnO, respectively. The results show that the branching of ZnO microrods reduces the average crystallite size value, which is calculated from the profile of the most intense peak using the Debye-Scherrer equation.

3.2. Density Functional Theory Calculations: Geometry Optimization and Structural Parameters

To obtain the optimized cell parameters and confirm the structural properties of the synthesized samples, density functional theory calculations were applied using the Cambridge Serial Total Energy Package (CASTEP) included in the Materials Studio software [23, 24].

The electronic exchange correlation potential was described within the generalized gradient approximation proposed by Perdew, Burke, and Ernzerhof (GGA-PBE) and ultra-soft pseudo-potential (USP). For geometry optimization, the total energy convergence value is within 1.0×10^{-5} eV/atom, and the maximum iteration is within 100. The maximum force and atomic displacement thresholds for shape optimization were 0.01 eV/Å and 0.005 Å, respectively. The Brillouin zone's k-point grid had a fixed energy cutoff of 600 eV and measured 10×10×9.

The structural parameters of ZnO and BZnO microrods after geometry optimization in the current work are presented in Table 2 and analyzed in comparison.

Our calculated structural parameters agree well with our experimental data and the values reported in ref. [25]. This consistency validates our DFT-based approach and increases our confidence in its reliability for these samples.

The branching process, as our calculations show, leads to a reduction in both the a and c lattice parameters. These reduced unit cell dimensions consequently lead to a significant shrinkage of the unit cell volume V. The bond length d_{Zn-O} between Zn and O atoms, which defines the anion-cation distance, is mainly influenced by this change in lattice parameters.

3.3. Scanning Electron Microscopy and Energy-Dispersive X-ray Spectroscopy Analysis

As shown in Fig. 3(a, b), SEM analysis revealed the presence of micrometer-sized rod-shaped structures in the ZnO layer deposited on the FTO substrate.

In the ZnO sample, ZnO microrods with multi-linked morphologies developed in high density were observed on the entire surface of the substrate. The ZnO microrods grown on the entire surface of the FTO substrate had a regular hexagonal shape with differently oriented smooth hexagonal facets and predominantly flat ends, which confirmed the XRD results [15].The ZnO rods were found as connected multipods.

Table 2. Comparison of lattice constants, unit cell volume, Oxygen z positions and the average bond length d_{Zn-O} using Rietveld analysis acquired from XRD with geometrical optimization by GGA-PBE functional

Samples	Ref (Present work)	$\mathbf{a = b}$ (Å)	**c** (Å)	**V** (Å^3)	$\mathbf{z_{Oxygen\ position}}$	$\mathbf{d_{Zn-O}}$ (Å)
ZnO microrods	Calculated values	3.28059	5.29496	49.351	0.37520	1.997
	Experimental values	3.24871	5.20592	47.583	0.37145	1.992
BZnO microrods	Calculated values	3.27671	5.29044	49.192	0.38842	1.999
	Experimental values	3.24853	5.20424	47.562	0.39795	1.949

[DOI: 10.22068/ijmse.3884]

The diameter of the rod is about 0.7-1 µm, and the length of the rod is about 4-5 µm. Fig. 3(c, d) shows that the morphology of the BZnO sample changed significantly as we observe the growth of the branches of the rods starting laterally on the surface and top of the trunk of the ZnO rods. SEM images reveal a novel structure of thin nanoscale branches arranged around microrods. The overall appearance resembles that of a branched ZnO microrod network. These rod-shaped structures have an average diameter of about 2-3 µm and an average length of about 5-7 µm. It can be seen that the diameter of the rods increases after the branching process. The SEM image shows that in the BZnO sample structure, there are some unconnected single ZnO microrods with regular hexagonal shape and flat ends, which are isolated and not connected to other rods or branches [26].

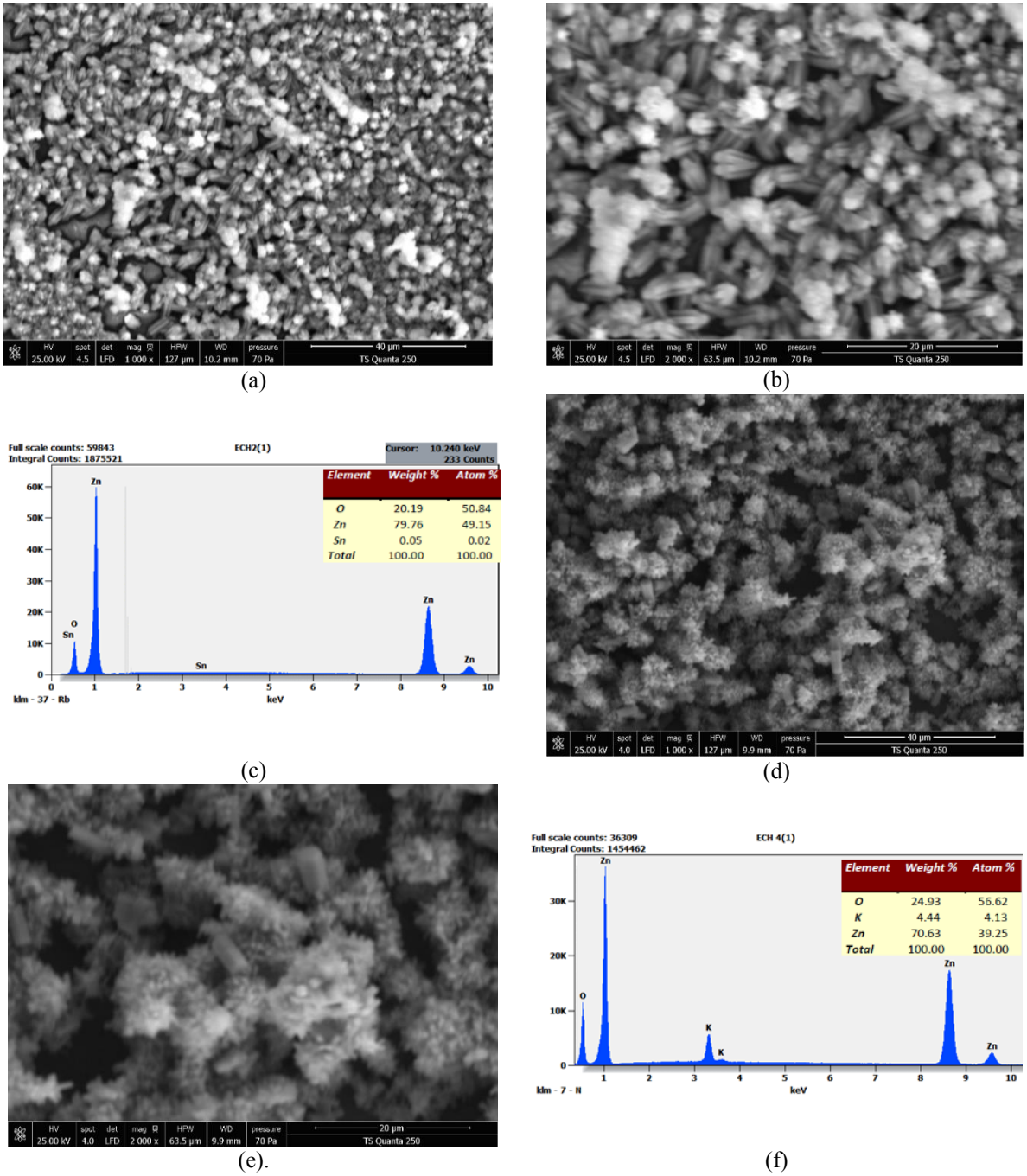

Fig. 3. Scanning Electron Microscopy images and Energy Dispersive X-Ray analysis results of ZnO (a,b,c) and BZnO microrods (d,e,f)

[DOI: 10.22068/ijmse.3884]

EDX analysis confirmed the elemental composition of the films. Fig. 3(c, f) shows the EDX spectra of the prepared ZnO and BZnO microrods. The EDX spectrum and table in Fig. 2(c) reveal the presence of zinc (Zn), oxygen (O), and tin (Sn) in the ZnO MRs sample. Similarly, the EDX spectrum of the BZnO sample (Fig. 3(f)) confirms the presence of zinc (Zn), oxygen (O), and potassium (K). For the ZnO microrod sample, EDX analysis shows an atomic ratio O/Zn close to stoichiometry (1.03) and a low tin (Sn) concentration (0.02%). Based on the XRD analysis, which shows the presence of a distinct SnO_2 phase, the most probable origin of the Sn is the FTO (Fluorine-doped Tin Oxide F: SnO_2) substrate used for the growth of the ZnO microrods. The EDX spectrum and table in Fig. 3(f) show a non-stoichiometric composition of the branched ZnO microrods. The high O/Zn ratio (56.62% oxygen and 39.25% zinc) indicates an excess of oxygen, which is probably caused by point defects in the crystal structure. Additionally, potassium (4.13%) is significant and likely originates from the KOH solution used in CBD synthesis during the branching process.

3.4. Fourier Transform Infrared Spectroscopy Analysis

Fourier transform infrared (FTIR) spectroscopy was employed to characterize the vibration modes of the prepared samples. The FTIR spectra of ZnO and BZnO samples were obtained in the range of 400 cm^{-1} to 4000 cm^{-1} and are shown in Fig. 4.

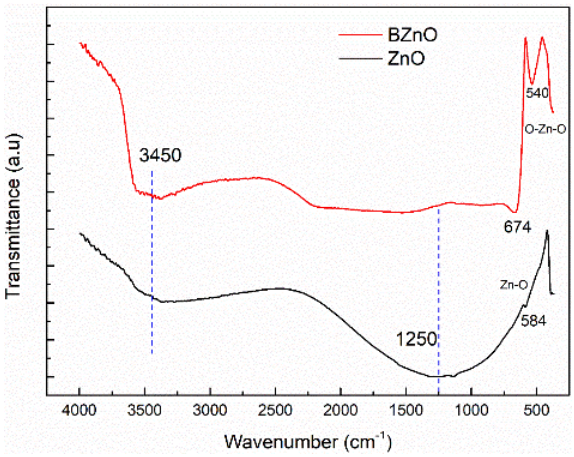

Fig. 4. FTIR spectra of ZnO and BZnO microrods

The FTIR analysis shows a clear and intense symmetrical vibration peak at around 540 cm□¹ only in the BZnO sample. This peak is attributed to O-Zn-O bonds [27]. The high intensity suggests a possible connection with the presence of excess oxygen, which could facilitate the formation of new O-Zn-O configurations and alter the environment of existing configurations. Furthermore, the observation of a new O-Zn-O vibrational mode at 540 cm^{-1} after the branching process is consistent with the increased oxygen content detected by EDX. This suggests a connection between the structural changes caused by branching and the chemical composition of the microrod.

The broad peak observed in both ZnO and BZnO samples at around 674 cm^{-1} was attributed to the Zn-O metal-oxygen stretching mode [28]. While the exact position may differ slightly between the two materials, separate peaks at 584 cm^{-1} and 674 cm^{-1} were assigned to ZnO and BZnO, respectively. This shows a clear blue position shift and broadening of the bands after the branching process. These findings confirm the significant impact of the branching process on the ZnO microrod structure, potentially leading to the formation of a new O-Zn-O bond or the modification of an existing bond. Furthermore, the broad and symmetrical band around 1250 cm^{-1} observed in the FTIR spectrum of the ZnO sample can be attributed to C-N stretching vibrations [29]. The origin of this band could be due to residual HMTA ($C_6H_{12}N_4$) used in preparing ZnO microrods, or even other impurities. The large width and symmetry suggest a distribution of chemical environments for the C-N bonds or even a superposition of multiple overlapping bands. Remarkably, the disappearance of this band after the branching process suggests a decrease in the concentration of C-N groups, a change in their chemical environment, or masking by newly formed bands.

Both infrared (IR) spectra have a broad band in the range of 3000–3500 cm^{-1}. This band is mainly due to the N-H stretching vibration at ~3250 cm^{-1}, which is present together with the O-H stretching vibration at ~3450 cm^{-1} [30]. The O–H stretching can be attributed to hydroxyl groups (OH) on the ZnO surface or adsorbed water molecules. The N-H stretching is likely due to residual zinc nitrate hexahydrate ($Zn(NO_3)_2 \cdot 6H_2O$) used to synthesise the ZnO microrods. After the branching process, the intensity of this bond increases, and the width decreases.

Excess oxygen affects the O-Zn-O and Zn-O vibrations as observed in FTIR spectra. The branching process plays a role in creating surface

[DOI: 10.22068/ijmse.3884]

defects and reactive sites that facilitate oxygen adsorption and the formation of new O-Zn-O bonds. Furthermore, branching can lead to rearrangements of oxygen atoms within the microrod structure, changing the environment of existing Zn-O bonds and potentially creating new configurations. These structural and compositional changes can profoundly affect the material's properties, including electrical conductivity, photoactivity and chemical reactivity. Compared to ZnO, the BZnO sample has a significantly increased vibration peak at 3450 cm^{-1}. This observation suggests enhanced oxygen adsorption on the BZnO surface, potentially leading to higher catalytic activity [27]. Furthermore, BZnO exhibits stronger Zn-O-Zn and O-H stretching bands compared to ZnO. These features likely contribute to the increased photoactivity of BZnO under UV/sunlight illumination. Alternatively, the ZnO sample may have lower photocatalytic activity, as indicated by the observed weak Zn-O-Zn band [27].

3.5. Raman Spectroscopy Study

To further confirm the hexagonal wurtzite structure of the ZnO and BZnO microrods, the Raman spectra of both samples are shown in Fig. 5.

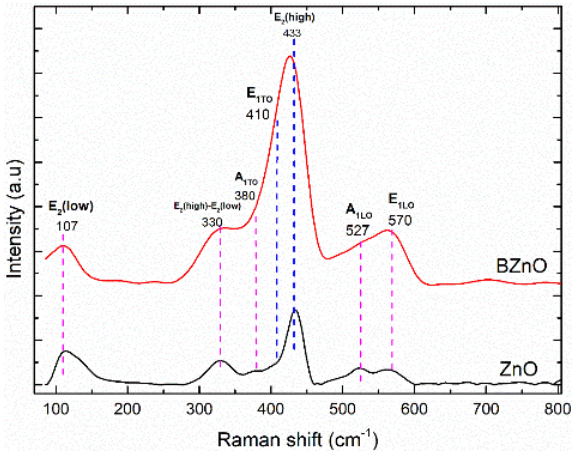

Fig. 5. Raman spectra of ZnO and BZnO microrods

Fig. 5 shows the Raman spectra of the BZnO and ZnO microrods recorded at room temperature in the range of 90–800 cm^{-1}. As shown in Fig. 5, the most intense Raman peak at 433 cm^{-1} was one of the characteristic peaks of wurtzite ZnO, which corresponds to the 1st order non-polar active Raman mode of ZnO E2 (high) associated with the vibration of O atoms in the ZnO lattice. The observed peaks at 107, 330, 380, 410, 525 and 570 cm^{-1} are the phonon modes E2 (low), E2 (high)-E2 (low), A1 (TO), E1 (TO), A1 (LO) and E1 (LO) [31, 32]. The 2nd order mode of E2 (high)-E2 (low) is due to interstitial defects in the atomic structure of ZnO. The appearance and position of these peaks confirm that the grown structures were wurtzite ZnO with high crystal quality [33]. In agreement with the XRD results, the Raman spectra show peaks corresponding to the phonon modes of hexagonal wurtzite ZnO. Fig. 5 also shows that the BZnO spectrum exhibits an increase in peak intensities as well as overall broadening for all vibrational modes in the 90–800 cm^{-1} range, particularly for the E1 (LO) and E2 (high) modes. The peak at 570 cm^{-1} is assigned to the E1(LO) mode due to impurities and structural defects such as oxygen vacancies V_O and Zn interstitials Zn [34, 35]. This observation is explained by an increase in the concentration of intrinsic defects in the branched microrods. This observation is consistent with the work of Liu et al. on ZnO nanorods after branching, where a similar increase in the intensity of the E1(LO) mode was also observed [36]. Raman spectroscopy analysis revealed a significant increase in the intensity of the E2 (high) mode and a broadening of all peaks, indicating a decrease in crystallite size and a higher concentration of defects within the branched microrods [37]. This is in perfect agreement with the XRD observations, indicating a reduction in the average crystallite size from 56.58 to 50.04 nm after the branching process.

The branching of ZnO microrods significantly affects their structural properties, mainly by reducing the crystallite size and increasing the defect concentration. This process breaks existing microrods and limits further crystallite growth by expanding the surface area. Furthermore, bond rearrangements during branching lead to new defects, and the larger surface area exposes more potential defect sites. These structural changes can influence various properties. For example, reduced crystallite size can reduce electrical conductivity, while increased defect concentration can improve chemical reactivity. Branching can also influence luminescence properties, making these microrods potentially valuable for catalysis and chemical sensing applications. Therefore, further research is essential to elucidate the specific types of defects created by branching and their influence on the optical behavior of the microrods.

[DOI: 10.22068/ijmse.3884]

3.6. UV–Visible Diffuse Reflectance Spectroscopy Analysis

Fig. 6 shows the absorption spectra of the prepared samples measured using UV-visible diffuse reflectance spectroscopy (UV-vis DRS). As Fig. 6(a) shows, both samples exhibit strong absorption in the UV region. This UV absorption is characteristic of electron-hole recombination in the ZnO conduction and valence bands [26]. The UV-visible light absorption spectrum shows a slight enhancement after the branching process. This phenomenon may be due to the combined effects of light scattering within the trunks and branches of the BZnO microrods [36]. The higher optical absorption in the visible region measured in the BZnO sample may be useful for the photocatalytic activity. Ebrahimi et al. also observed this effect with branched nanowires and nanorods [31, 36]. Notably, the branched sample shows a red shift of the absorption edge to longer wavelengths. This phenomenon occurs due to a reduction in the energy gap between the conduction and valence bands. Bulk ZnO is known to have an absorption edge in the UV-visible spectrum at around 368 nm [38]. This wavelength is proven to be longer (higher wavelength) compared to the absorption edges observed in our as-prepared ZnO microrods (392 nm) and branched microrods (401 nm). This phenomenon, known as the blue shift, may be due to the size effect. Essentially, the bandgap energy increases as the particle size decreases (as in our microrods), leading to the absorption of higher energy (shorter wavelength) photons. This explains the observed blue shift of the absorption edge of our ZnO and BZnO microrods compared to bulk ZnO [39].

Tauc plots are employed to determine the bandgap E_g of the semiconductor. Our approach exploits the established relationship between the UV-Vis absorption coefficient α, the photon energy hν and the semiconductor band gap E_g, as described by equation (2) [40]:

$$(\alpha h\nu)^{1/n} = k(h\nu - E_g) \quad (2)$$

Here, h represents Planck's constant (6.626 10^{-34} Js), and ν denotes the frequency of the incident photon (s^{-1}) and k represents a proportionality constant. For direct and indirect bandgap semiconductors, n is a factor equal to 1/2 and 2, respectively.

The band gap (Eg) was obtained from the Tauc [40] plot of $(\alpha h\nu)^2$ as a function of the photon energy (hν), as shown in insert Fig. 6(b, c).

The measured optical band gap energy values of ZnO and BZnO samples are 3.19 and 3.17 eV, respectively, which is lower than the value reported for bulk ZnO (3.37 eV) and comparable to that reported by Jalolov et al. found value (3.22 eV) [2].

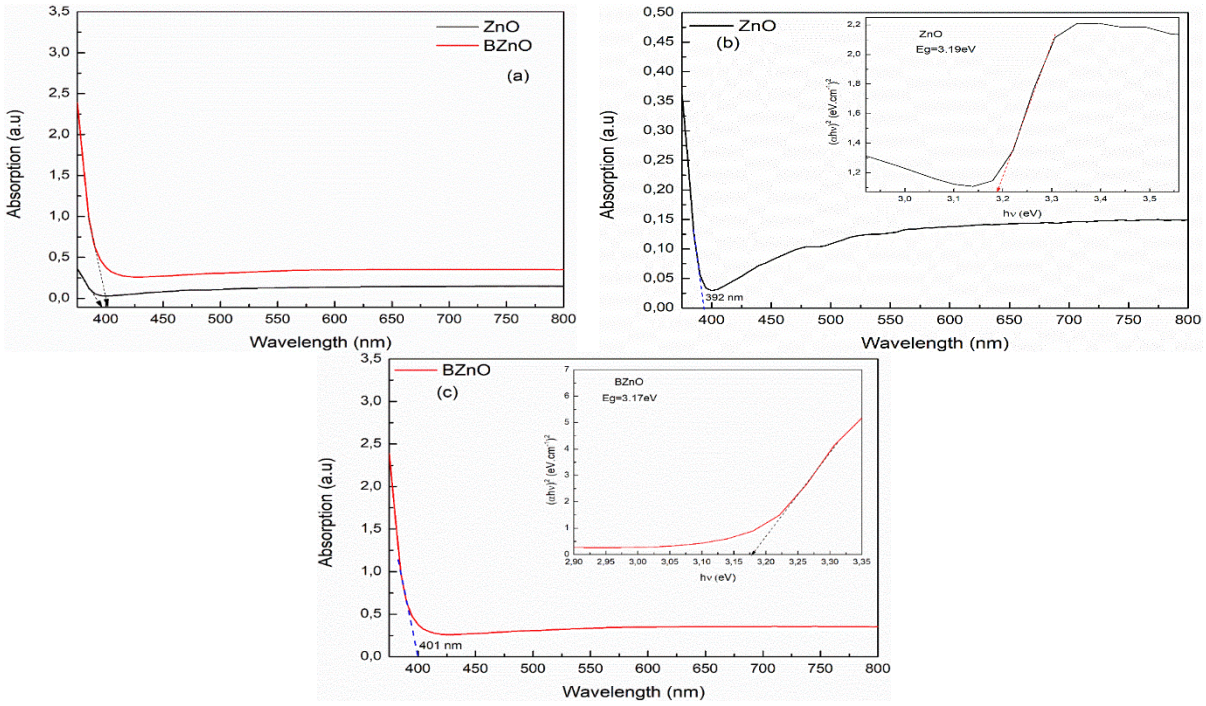

Fig. 6. UV-visible absorbance spectra of ZnO and BZnO microrods a) and their band gap energies of Tauc's plot b, c) insert

[DOI: 10.22068/ijmse.3884]

Based on the results of EDX and FTIR analyses, the observed band gap shift in the branched microrods could be related to the oxygen content on their surface. Previous studies have shown that oxygen-rich BZnO samples tend to have lower bandgap values than ZnO [41]. Since defects within the material can influence bandgap changes, photoluminescence characterization is required to investigate the presence and nature of these defects in the branched microrods.

3.7. Photoluminescence Study

Photoluminescence spectroscopy provides valuable insights into the optical properties, material quality, and the presence of defects in semiconductors [42]. By measuring the different transition energies within the material, photoluminescence can be used to assess the separation efficiency of photogenerated electron-hole pairs [43]. Here, we investigate the PL spectra of the synthesized samples measured at room temperature under 325 nm excitation. As shown in Fig. 7(a), both samples exhibit a broad PL band from 300 nm to 650 nm.

It is noteworthy that the PL intensity of this band decreases significantly after the branching process, which was also reported by Liu et al. in ZnO nanorods [36]. This decrease can be attributed to the formation of defects and traps on the surfaces of the microrods during branching. These defects have two main effects on the optical properties of ZnO microrods. First, they enhance the absorption of ultraviolet and visible light, which explains the increased absorption observed in Fig. 7(a). This amplification occurs because the defects introduce new energy levels within the bandgap, allowing them to trap incoming photons. Second, these defects act as non-radiative recombination centers for electron-hole pairs. This creates a competing pathway for energy relaxation that does not involve light emission. Consequently, the radiative recombination responsible for the PL signal is reduced, leading to decreased PL intensity.

To better understand the electron-hole transition mechanisms involved, the PL spectra were deconvoluted using Gaussian analysis (Fig. 7(b) and 7(c)). The deconvolution shows that both samples have similar emission peaks, but different intensities, peak widths and slightly different peak energies.

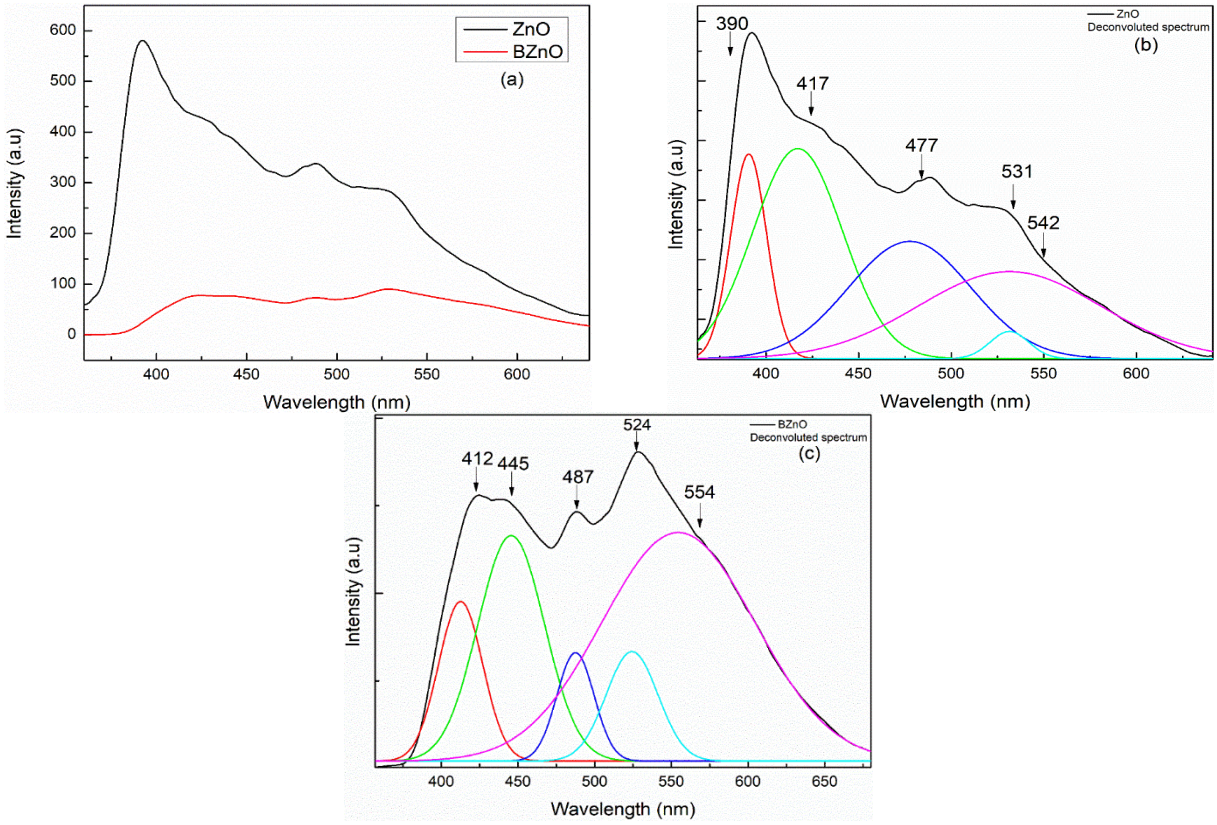

Fig. 7. a) Photoluminescence spectra of ZnO and BZnO microrods. b, c) Deconvolution of Photoluminescence spectra of ZnO and BZnO samples

[DOI: 10.22068/ijmse.3884]

The PL spectrum of the ZnO microrods shows a UV emission peak centered at 390 nm (3.179 eV). This peak is attributed to Near-Band Edge (NBE) emissions, which typically arise from excitonic or band-to-band electron-hole recombinations in ZnO [38]. As shown in Fig. 7(c), the NBE emission of ZnO shifted to longer wavelengths from 390 nm to 412 nm (3.001 eV), which is due to the unique morphology and special growth conditions of branched ZnO microrods. This significant shift observed in BZnO indicates a reduced band gap. This leads to easier electron excitation, which may have implications for photocatalysis. Since exciton formation is crucial for photocatalysis but is limited by recombination, the reduced band gap in BZnO implies a reduced recombination rate. This could lead to longer-lived excitons and ultimately improve photocatalytic performance. These results indicate that BZnO is a promising candidate for further research on photocatalysis [36].

In addition to the observed NBE emission from ZnO, both samples showed four additional emissions in the visible region. These emissions probably originate from radiative recombination processes involving point defects in the zinc oxide (ZnO) lattice. In particular, the presence of interstitial zinc defects (Zn_i) and zinc vacancy defects (V_{Zn}), as well as oxygen vacancy defects (V_O), could explain the observed visible photoluminescence.

The violet emission observed in ZnO (around 417 nm) and BZnO (around 445 nm) probably originates from the electron transition energy from the conduction band to the V_{Zn} as a shallow acceptor levels of zinc vacancy, or to the transition energy from Zn_i as a shallow donor levels of zinc interstitial to the valence band**.** The blue emission at 477 and 487 nm for ZnO and BZnO, respectively, is attributed to the electronic transition energy between Zn_i as a shallow donor level of zinc interstitial and V_{Zn} as acceptor levels of zinc vacancy, and the electronic transition between Zn_i levels and the valence band. The observed green luminescence emissions in ZnO (at 531 and 542 nm) and BZnO (at 524 and 554 nm) probably arise from electronic transitions from ionized oxygen vacancies V_{O+} level to the valence band [44].

Photoluminescence (PL) analysis shows a stronger green emission peak in BZnO microrods than ZnO microrods, suggesting a higher concentration of oxygen-related defects. Based on our observations, we hypothesize that the branching process correlates with increased oxygen-related defects. This is consistent with SEM, FTIR, Raman and UV-visible spectroscopy observations. These defects can enhance photodegradation performance by facilitating the adsorption of oxygen molecules on the BZnO surface. This improved oxygen adsorption is believed to be a key factor for the enhanced photocatalytic activity of BZnO [36, 45]. The observed decrease in PL intensity across all frequencies for BZnO is a positive indicator of photocatalytic activity. This decrease indicates increasing separation of the photogenerated electron-hole pairs. Efficient charge separation is crucial in photocatalysis. Separated charges have a longer (exciton lifetime) before recombining, allowing more reduction and oxidation reactions to occur on the catalyst surface, ultimately leading to improved photocatalytic performance. Therefore, the branched ZnO microrods with reduced recombination offer greater potential for photocatalytic applications than simple ZnO microrods.

4. CONCLUSIONS

In the present study, a three-step synthesis method was used to synthesize branched ZnO microrod structures. XRD data, Rietveld refinement and Raman confirmed that the prepared samples exhibited a pure hexagonal wurtzite structure. Density functional theory calculations showed excellent agreement with the experimental lattice parameters, increasing the reliability of the results. Photoluminescence analysis suggests that these BZnO microrods have a higher concentration of oxygen-related defects than the unbranched ZnO microrods. These defects, further confirmed by XRD, SEM, FTIR, Raman and UV-Vis spectroscopy, are believed to enhance the photocatalytic activity by facilitating the adsorption of oxygen molecules on the BZnO microrod surface. Furthermore, the observed decrease in PL intensity across all frequencies for BZnO suggests improved separation of the photogenerated electron–hole pairs, another crucial factor for efficient photocatalysis. These results highlight the promising potential of branched ZnO microrods for photocatalytic applications, particularly in degrading organic pollutants under UV and solar light. The branched architecture offers key advantages over conventional ZnO microrods, including increased surface area

[DOI: 10.22068/ijmse.3884]

for reactant adsorption, enhanced light harvesting due to multiple scattering within the branches, and more efficient charge separation. Such improvements can lead to higher photocatalytic efficiency and faster pollutant degradation rates. Future work will focus on optimizing their performance for specific photocatalytic processes and scaling up their practical application in water treatment systems.

REFERENCES

[1] Choi, S.C., D.K. Lee, and S.H. Sohn, Nanomaterials, (2021). DOI: https://doi.org/10.3390/nano11102518.

[2] Jalolov, R.R., et al., Physica B: Condensed Matter, (2024). DOI: https://doi.org/10.1016/j.physb.2023.415613.

[3] Ahmed, A.P.D.N., et al., Photonics, (2023). DOI: 10.3390/photonics10080910.

[4] Rhouma, F.I.H., et al., Vacuum, (2023). DOI: https://doi.org/10.1016/j.vacuum.2023.112424.

[5] Ahmed, N.M., et al., Photonics, (2023). DOI: 10.3390/photonics10080910.

[6] Benu, D.P., et al., New Journal of Chemistry, (2023). DOI: 10.1039/D2NJ04862K.

[7] Ahmedbowba, S., et al., (2025). DOI: https://doi.org/10.48550/arXiv.2503.02731.

[8] Mastour, N., et al., Eur. Phys. J. Plus, (2022). DOI: https://doi.org/10.1140/epjp/s13360-022-03351-w.

[9] Mrabet, C., et al., Materials Science and Engineering: B, (2024). DOI: https://doi.org/10.1016/j.mseb.2023.117130.

[10] Yang, Y., et al., Surfaces and Interfaces, (2024). DOI: https://doi.org/10.1016/j.surfin.2024.104131.

[11] Arab Chamjangali, M., et al., Spectrochim Acta A Mol Biomol Spectrosc, (2015). DOI: 10.1016/j.saa.2015.05.067.

[12] Anas, S., R.V. Mangalaraja, and S. Ananthakumar, J Hazard Mater, (2010). DOI: 10.1016/j.jhazmat.2009.10.093.

[13] Witkowski, B., Acta Physica Polonica, A., (2018).

[14] Siriphongsapak, N. and S. Denchitcharoen, Materials Research Express, (2022). DOI: 10.1088/2053-1591/ac6794.

[15] Koyasu, S., et al., Langmuir, (2023). DOI: 10.1021/acs.langmuir.2c02734.

[16] Yang, W., et al., Journal of Alloys and Compounds, (2021). DOI: https://doi.org/10.1016/j.jallcom.2020.158410.

[17] Rodríguez-Carvajal, J., Physica B: Condensed Matter, (1993). DOI: https://doi.org/10.1016/0921-4526(93)90108-I.

[18] Rhouma, F.I.H., et al., Chinese Journal of Physics, (2021). DOI: https://doi.org/10.1016/j.cjph.2020.09.038.

[19] Abushad, M., et al., AIP Conference Proceedings, (2020). DOI: 10.1063/5.0017057.

[20] Upadhaya, D. and D. Dhar Purkayastha, Ceramics International, (2020). DOI: https://doi.org/10.1016/j.ceramint.2020.03.130.

[21] Mahroug, A., et al., Optical Materials, (2023). DOI: https://doi.org/10.1016/j.optmat.2023.114043.

[22] Cullity, B.D., Elements of x-ray diffraction. Second edition ed. Addison-Wesley series in metallurgy and materials. 1978, Reading, MA: Addison-Wesley Publishing Company, Inc.

[23] Clark, S.J., et al., Zeitschrift für Kristallographie-Crystalline Materials, (2005). DOI: 10.1524/zkri.220.5.567.65075.

[24] Bardaoui, A., et al., Journal of Solid State Chemistry, (2024). DOI: https://doi.org/10.1016/j.jssc.2024.124732.

[25] Moin, M., et al., Journal of Molecular Modeling, (2023). DOI: 10.1007/s00894-022-05425-z.

[26] Empizo, M.J.F., et al., Optical Materials, (2017). DOI: https://doi.org/10.1016/j.optmat.2016.09.004.

[27] Zuo, D., et al., Coatings, (2024). DOI: https://doi.org/10.3390/coatings14020192.

[28] Krajian, H., et al., Microelectronics Reliability, (2021). DOI: https://doi.org/10.1016/j.microrel.2021.114352.

[29] Idiawati, R., et al., IOP Conference Series: Materials Science and Engineering, (2017). DOI: 10.1088/1757-899X/202/1/012050.

[30] Kim, K.H., et al., Superlattices and Microstructures, (2016). DOI: https://doi.org/10.1016/j.spmi.2016.01.019.

[31] Ebrahimi, M., et al., Applied Surface Science, (2018). DOI: https://doi.org/10.1016/j.apsusc.2017.11.052.

[32] Evstafieva, M., et al., Materials, (2024). DOI: https://doi.org/10.3390/ma17051053.

[33] Kiriarachchi, H.D., et al., ACS Omega, (2019). DOI: 10.1021/acsomega.9b01772.

[34] Perhaţia, I., et al., Colloids and Surfaces A:

[DOI: 10.22068/ijmse.3884]

Physicochemical and Engineering Aspects, (2024). DOI: https://doi.org/10.1016/j.colsurfa.2023.133102.
[35] Shakti, N., et al., Hybrid Advances, (2024). DOI: https://doi.org/10.1016/j.hybadv.2023.100124.
[36] Liu, Y., N. Zhao, and W. Gao, RSC Advances, (2013). DOI: 10.1039/C3RA42902D.
[37] Ojha, A.K., et al., Vibrational Spectroscopy, (2014). DOI: https://doi.org/10.1016/j.vibspec.2014.02.013.
[38] Zhang, L., et al., Inorganic Chemistry, (2013). DOI: 10.1021/ic401646t.
[39] Salazar, K.A., et al., Journal of Crystal Growth, (2021). DOI: https://doi.org/10.1016/j.jcrysgro.2021.126332.
[40] Tauc, J., Physics Today, (1976). DOI: 10.1063/1.3024406.
[41] Adaikalam, K., et al., Journal-Korean Physical Society, (2009). DOI: 10.3938/jkps.55.2476.
[42] Dhifallah, I., et al., Eur. Phys. J. Appl. Phys., (2009). DOI: https://doi.org/10.1051/epjap/2009107.
[43] Dhifallah, I., et al., Journal of Luminescence, (2011). DOI: https://doi.org/10.1016/j.jlumin.2011.01.012.
[44] Berra, S., et al., Optical Materials, (2022). DOI: https://doi.org/10.1016/j.optmat.2022.113188.
[45] Liao, F., et al., Journal of Materials Science: Materials in Electronics, (2017). DOI: 10.1007/s10854-017-7602-2.

[DOI: 10.22068/ijmse.3884]